The Astronomical Journal, 168:247 (11pp), 2024 December https://doi.org/10.3847/1538-3881/ad7fce

Lunar Farside Samples Returned by Chang'E-6 Mission: Significance for Understanding the South Pole-Aitken Basin Stratigraphic History

Xing Wang[1,2,3], James W. Head[2], Wenhao Zhao[2], Yuan Chen[3], Qin Zhou[3], Jiaming Zhu[1], Bo Wu[1], Jianjun Liu[3,4], and Chunlai Li[3,4]

[1] Planetary Remote Sensing Laboratory, Department of Land Surveying and Geo-Informatics, The Hong Kong Polytechnic University, Hung Hom, Hong Kong; bo.wu@polyu.edu.hk
[2] Department of Earth, Environmental and Planetary Sciences, Brown University, Providence, RI, USA; James_Head@brown.edu
[3] Key Laboratory of Lunar and Deep Space Exploration, National Astronomical Observatories, Chinese Academy of Sciences, Beijing, People's Republic of China; liujj@nao.cas.cn
[4] School of Astronomy and Space Science, University of Chinese Academy of Sciences, Beijing, People's Republic of China
Received 2024 August 19; revised 2024 September 18; accepted 2024 September 23; published 2024 November 11

Abstract

The Chang'E-6 (CE-6) mission, launched by China on 2024 May 3, marks the first successful retrieval of samples from the farside of the Moon, specifically from the southern mare plain of the Apollo basin within the South Pole-Aitken (SPA) Basin. This study aims to provide a comprehensive geological analysis of the Apollo basin, focusing on the Apollo basin materials that CE-6 may have collected. By examining the regional geology, surface mineralogy, thorium (Th) abundance, and crustal thickness, we seek to understand the implications of these materials for the SPA basin's structure and stratigraphic history. We find that the Apollo basin exhibits significant lateral compositional variations, with Mg-rich noritic materials predominantly in the southwestern portion and more feldspathic materials in the northeast, probably due to the fact that the Apollo basin is situated on different structures of the underlying SPA basin. Those Mg-rich materials, likely representing deep lithologies from local lower crust, are associated with low Th abundance, suggesting a KREEP-poor origin. The inclusion of foreign materials in the CE-6 samples increases the complexity while also enhancing their research potential. In addition to the local mare basalts, Mg-rich noritic materials associated with the Apollo basin and Th-rich materials originating from the SPA basin may also have been collected by CE-6. Laboratory research of these diverse lithologies will contribute to unraveling the characteristics of the farside mantle, the geological history of the giant SPA basin, as well as the cause of the substantial asymmetry between the lunar nearside and farside.

Unified Astronomy Thesaurus concepts: The Moon (1692); Lunar composition (948); Lunar mineralogy (962); Lunar interior (959); Lunar craters (949)

Materials only available in the online version of record: data behind figure

1. Introduction

Humans have never retrieved samples from the enigmatic farside of the Moon until China launched the landmark Chang'E-6 (CE-6) probe on 2024 May 3. Initially designed as the backup of CE-5 (C. Zhou et al. 2022), which had successfully returned sample from lunar nearside in 2020 (e.g., Y. Qian et al. 2021), CE-6 was repurposed with an ambitious new task: to collect and bring the first samples from the farside of the Moon back to Earth. Early in the morning of June 2 (6:23 a.m. Beijing Time), CE-6 successfully landed on the southern mare plain of the Apollo basin interior, in the northeast corner of the farside South Pole-Aitken (SPA) basin (Figure 1). Over the following two days, the lander conducted ground operations, including sampling (both scooping and drilling), depositing and sealing the samples in the ascent vehicle, and scientific investigations using the experiment payloads onboard the lander. Afterwards, the ascender transferred the sample container to orbiter-returner combination, which is responsible for returning the collected samples to Earth. On June 25, the sample return vehicle landed safely at the Siziwang Banner (Inner Mongolia, China), completing this 53 days robotic sample return mission to the farside of the Moon, bringing back the first-ever lunar farside samples with a total weight of ~1935.3 g (C. Li et al. 2024).

The CE-6 landing area was preliminarily divided into three subregions (designated F, L, and B by X. Zeng et al. 2023 as representing the northwest Flat plain, the northeast Low plain and the southwest Base plain, respectively) before launch (Figure 1(b)). Regions F and L are situated within the southern mare plain of the Apollo basin, while region B lies outside the Apollo basin, adjacent to its southern rim. Region B is also part of the central South Pole-Aitken compositional anomaly defined by D. P. Moriarty & C. M. Pieters (2018), which likely represents the cryptomare deposits in the SPA basin center (e.g., J. L. Whitten & J. W. Head 2015; X. Wang et al. 2024a). CE-6 eventually landed at the eastern part of region F, with coordinates of 41.625°S, 153.978°W (based on the digital orthophoto model (DOM) data of CE-2; C. Li et al. 2024). As pointed out by X. Zeng et al. (2023), in this region, CE-6 has the potential to collect lunar farside mare basalts, possibly including the older low-Ti basalt and the younger high-Ti basalt (Y. Qian et al. 2024), as well as small amounts of nonmare ejecta (Z. Jia et al. 2024; X. Wang et al. 2024b; Z. Yue et al. 2024). Although the absolute model age (AMA) of this region derived from crater size-frequency distribution (CSFD) measurements varies in different studies (e.g., R. Greeley et al. 1993; J. Haruyama et al. 2009; J. H. Pasckert

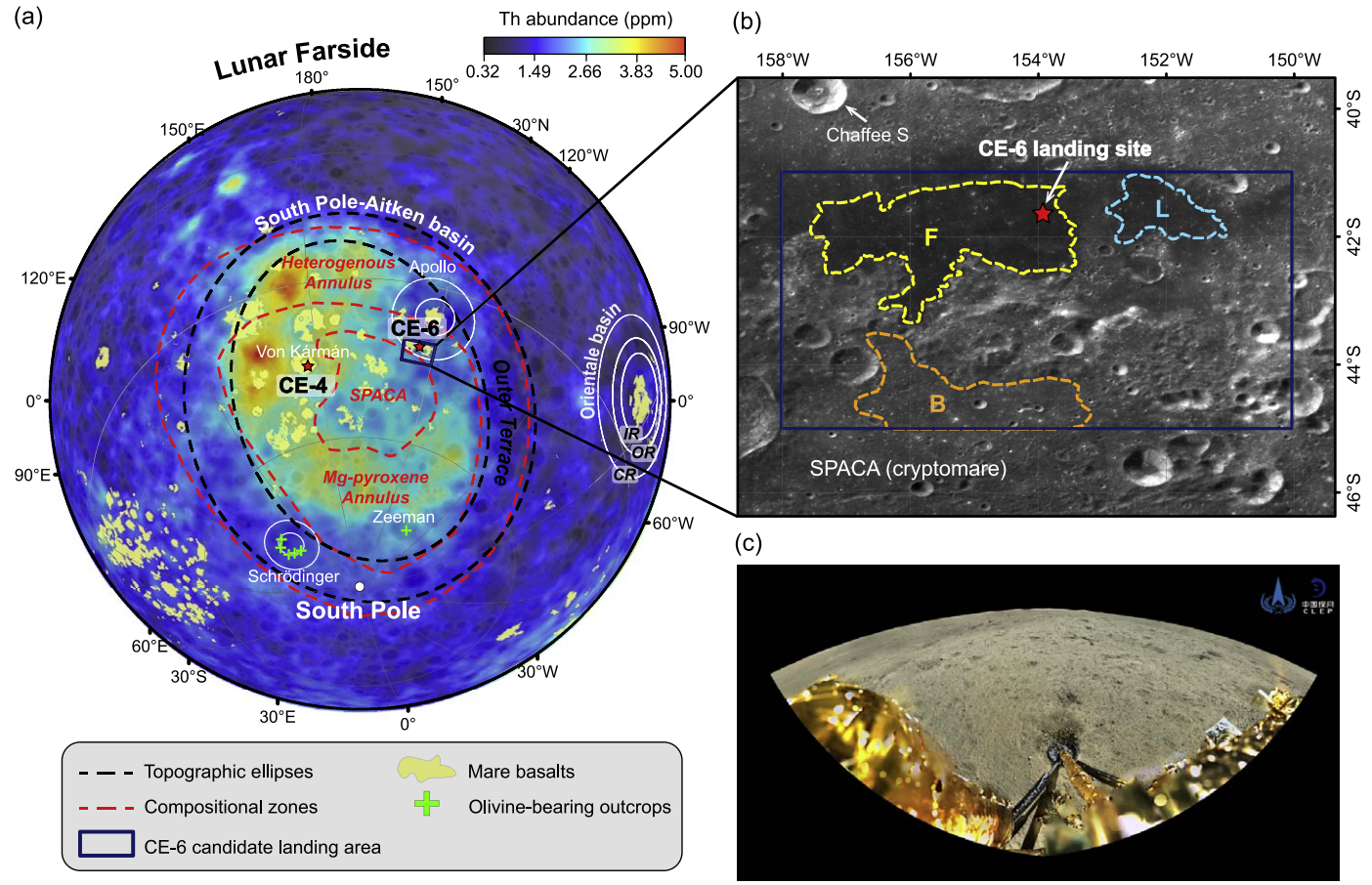

Figure 1. CE-6 landing site in the southern mare plain of the Apollo basin within the SPA basin. (a) shows the thorium distribution across the SPA basin (D. J. Lawrence et al. 2003). The red dashed lines are the boundaries of the SPA compositional zones proposed by D. P. Moriarty & C. M. Pieters (2018), and the black dashed lines represent the elliptical structure of the SPA basin (I. Garrick-Bethell & M. T. Zuber 2009). The white solid lines outline the locations and the ring systems of the Apollo basin, the Schrödinger basin and the Orientale basin (IR = Inner Rook ring, OR = Outer Rook ring, CD = Cordillera ring; J. W. Head 1974), respectively. The box in deep blue indicates the previous candidate CE-6 landing area (X. Zeng et al. 2023) and the red star is the final landing site. The green crosses are the locations of the olivine outcrops within the SPA basin identified by S. Yamamoto et al. (2012). The mare boundaries are from D. M. Nelson et al. (2014). Orthographic projection centered at the center of SPA basin (191.1°E, 53.2°S; I. Garrick-Bethell & M. T. Zuber 2009) is applied in (a). (b) The zoom-in CE-2 digital orthophoto model (DOM) image (C. Li et al. 2018) for the CE-6 landing area, which was previously divided into three subregions (F, L, and B). The image is in equirectangular projection. (c) A panoramic image of the landing site taken by a camera onboard the CE-6 lander before scoop sampling.

Table 1
CSFD Dating Results of the CE-6 Landing Area (Subregion F) in Different Studies

Reference	Production Function	Chronology Function	Absolute Model Age
R. Greeley et al. (1993)	G. Neukum (1983)	G. Neukum (1983)	$3.63^{+0.05}_{-0.06}$
J. Haruyama et al. (2009)	G. Neukum (1983)	G. Neukum (1983)	2.44
J. H. Pasckert et al. (2018)	G. Neukum et al. (2001)	G. Neukum et al. (2001)	$3.31^{+0.02}_{-0.02}$
X. Zeng et al. (2023)	G. Neukum (1983)	G. Neukum (1983)	$2.40^{+0.11}_{-0.11}$
Y. Qian et al. (2024)	G. Neukum et al. (2001)	Z. Yue et al. (2022)	$3.07^{+0.07}_{-0.08}$
Y. Wang et al. (2024c)	G. Neukum et al. (2001)	Z. Yue et al. (2022)	$2.49^{+0.072}_{-0.073}$
Z. Yue et al. (2024)	G. Neukum et al. (2001)	Z. Yue et al. (2022)	$2.50^{+0.078}_{-0.080}$

et al. 2018; X. Zeng et al. 2023; Y. Qian et al. 2024; Y. Wang et al. 2024c; Z. Yue et al. 2024; summarized in Table 1), most of them suggest that the volcanic activity could be younger relative to the Imbrian-aged peak of the mare basalt eruptions on the lunar nearside (~3.6–3.8 Ga; H. Hiesinger et al. 2000), probably occurring in the Late Imbrian Period or the Eratosthenian Period. C. M. Poehler et al. (2020), M. A. Ivanov et al. (2018), and C. Orgel et al. (2024) have mapped the detailed geology of this southern mare province of the Apollo basin, and C. Orgel et al. (2024) also provided the potential subsurface stratigraphy and the corresponding thickness of each layer.

As the largest and deepest confirmed basin on the Moon (e.g., P. D. Spudis et al. 1994; N. E. Petro & C. M. Pieters 2004), the ancient SPA basin has long been acknowledged as a window for studying the deep lunar interior (e.g., H. J. Melosh et al. 2017). Its ancient age (~4.2–4.3 Ga; H. Hiesinger et al. 2012) also suggests that it could reveal valuable insights into early solar system cratering chronology and early lunar thermal evolution. While the entire SPA basin has undergone extensive

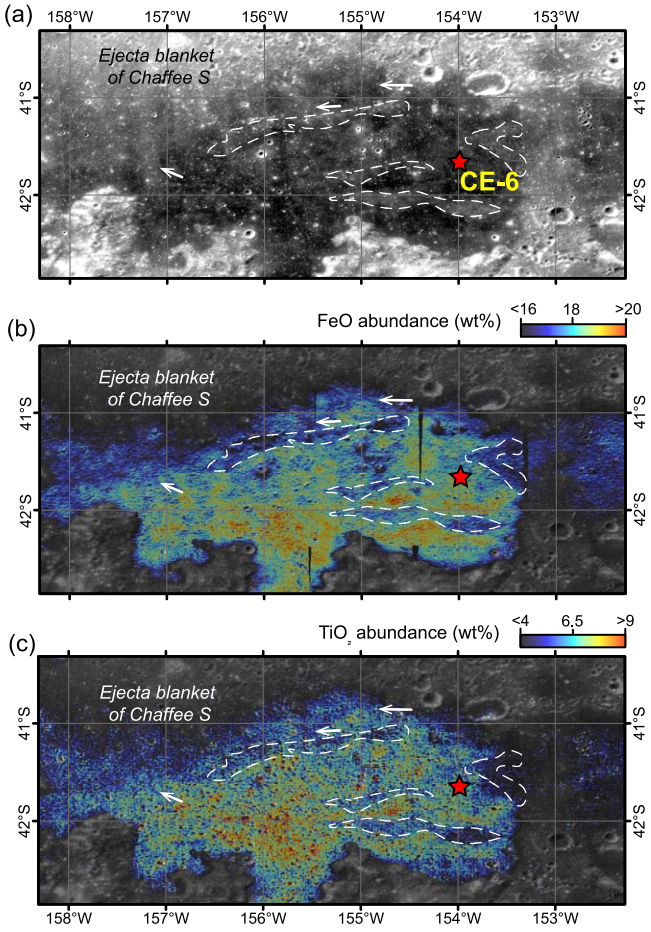

Figure 2. Distribution of foreign ejecta in the CE-6 landing area. (a) Grayscale stretched CE-2 DOM image (C. Li et al. 2018). The red star marks the final location of the CE-6 landing site. Some amounts of impact rays with higher albedo relative to surroundings can be observed. The arrows indicate some ejecta rays extending further from the Chaffee S ejecta blanket, and the white dashedes outline some ejecta rays from other sources in the near east–west direction. (b) and (c) display the iron (M. Lemelin et al. 2015) and titanium (H. Sato et al. 2017) abundance in the CE-6 landing area, respectively. In addition to the ejecta blanket of the Chaffee S, the bright ejecta rays originated from other sources also exhibit clear decreases in in iron and titanium abundances.

modification, investigations of post-SPA impact basins within SPA could still contribute to the understanding and reconstruction of the SPA stratigraphy. The 492 km diameter (D. M. H. Baker et al. 2011) Apollo peak-ring basin, the landing target of the CE-6 mission, is one such post-SPA basin. On the surface of region F, considerable amounts of ejecta rays showing higher albedo and lower iron and titanium abundances can be observed (Figure 2), suggesting that some nearby young craters, especially crater Chaffee S (Z. Jia et al. 2024; X. Wang et al. 2024b; Z. Yue et al. 2024), could have delivered some Apollo basin materials or even some SPA basin materials onto the CE-6 landing site. Compared to CE-5, the samples collected by CE-6 could be more diverse in lithological types due to more complex geological contexts, and these nonmare materials involved will significantly enlarge the studies of the CE-6 samples.

While comprehensive analysis of the mare deposits in and around the Apollo basin has been provided by some previous works (e.g., J. H. Pasckert et al. 2018; Y. Qian et al. 2024; X. Wang et al. 2024a; Y. Wang et al. 2024c), our work studies the remaining part of the Apollo basin from multiple perspectives (e.g., regional geology, distribution of compositions, thorium (Th) abundance, crustal thickness, etc.), with a focus on the Apollo basin materials that could have been collected by CE-6. We also place these Apollo basin materials into the context of the entire SPA basin to understand their implications for the SPA structure and stratigraphic history. Our work will provide additional guidance for the future laboratory analysis of the foreign materials in the CE-6 returned samples.

2. Data Sets and Data Processing

2.1. Data Sets

Topography data employed in this study is from SLDEM2015 (combined data from SELENE Terrain Camera and Lunar Orbiter Laser Altimeter; M. K. Barker et al. 2016; Figure 3(b)). Our mineralogical analysis (Figure 3(c)) relies on Moon Mineralogy Mapper (M^3) level 2 reflectance data (C. M. Pieters et al. 2009; J. W. Boardman et al. 2011; R. O. Green et al. 2011) primarily collected during optical period 2C2 and supplemented by OP2C3. Lithological analysis (Figure 5) is based on the mineral abundance maps derived from Kaguya Multiband Imager (MI) data (M. Ohtake et al. 2008; M. Lemelin et al. 2019). We also used the MI-derived iron abundance map (M. Lemelin et al. 2015) and the titanium abundance map acquired from LROC Wide Angle Camera data (H. Sato et al. 2017; Figure 2(c)). The Th distribution map is from Lunar Prospector gamma-ray spectrometer data (D. J. Lawrence et al. 2003, Figure 3(d)). Variations in crustal thickness were obtained from data derived from the Gravity Recovery and Interior Laboratory mission (M. A. Wieczorek et al. 2013; M. T. Zuber et al. 2013; Figure 3(e)). All of the data described above are available in the NASA Planetary Data System. The basemap image used throughout this paper is from the CE-2 DOM data (C. Li et al. 2018; Figure 3(a)).

2.2. Spectral Parameters and Classification

The M^3 spectra were first smoothed using the Savitzky–Golay algorithm (A. Savitzky & M. J. E. Golay 1964) with seven points and third polynomial order. Then the convex hull method was adopted to remove the continuums of the spectra (R. N. Clark & T. L. Roush 1984). Fourth-order polynomials were used to fit the continuum-removed spectrum around the 1 and 2 μm absorption regions. The band depths were obtained by subtracting the minima of the fitted line from 1, and the wavelengths corresponding to the minima of the fitted lines were regarded as the band centers. On the basis of these derived spectral parameters, we performed a spectral classification in order to further identify the surface components exposed in and around the Apollo basin. The classification rules and corresponding interpretations are shown in Table 2, and the result is shown in Figure 3. For the band centers, we selected 2 and 2.5 μm as the interval bands for spectral classification. Based on a series of studies on the variation of pyroxene compositions with respect to band centers (R. L. Klima et al. 2007, 2008, 2011a, 2011b), it is known that a pyroxene spectrum with the 2 μm band center less than 2 μm indicates its composition of othopyroxene or low-Ca clinopyroxene, which are close to the enstatite (En) endmember in the pyroxene quadrilateral (see Figure 13 in R. L. Klima et al. 2011a); if its 2 μm band center greater than 2 μm but less than 2.15 μm, the pyroxene

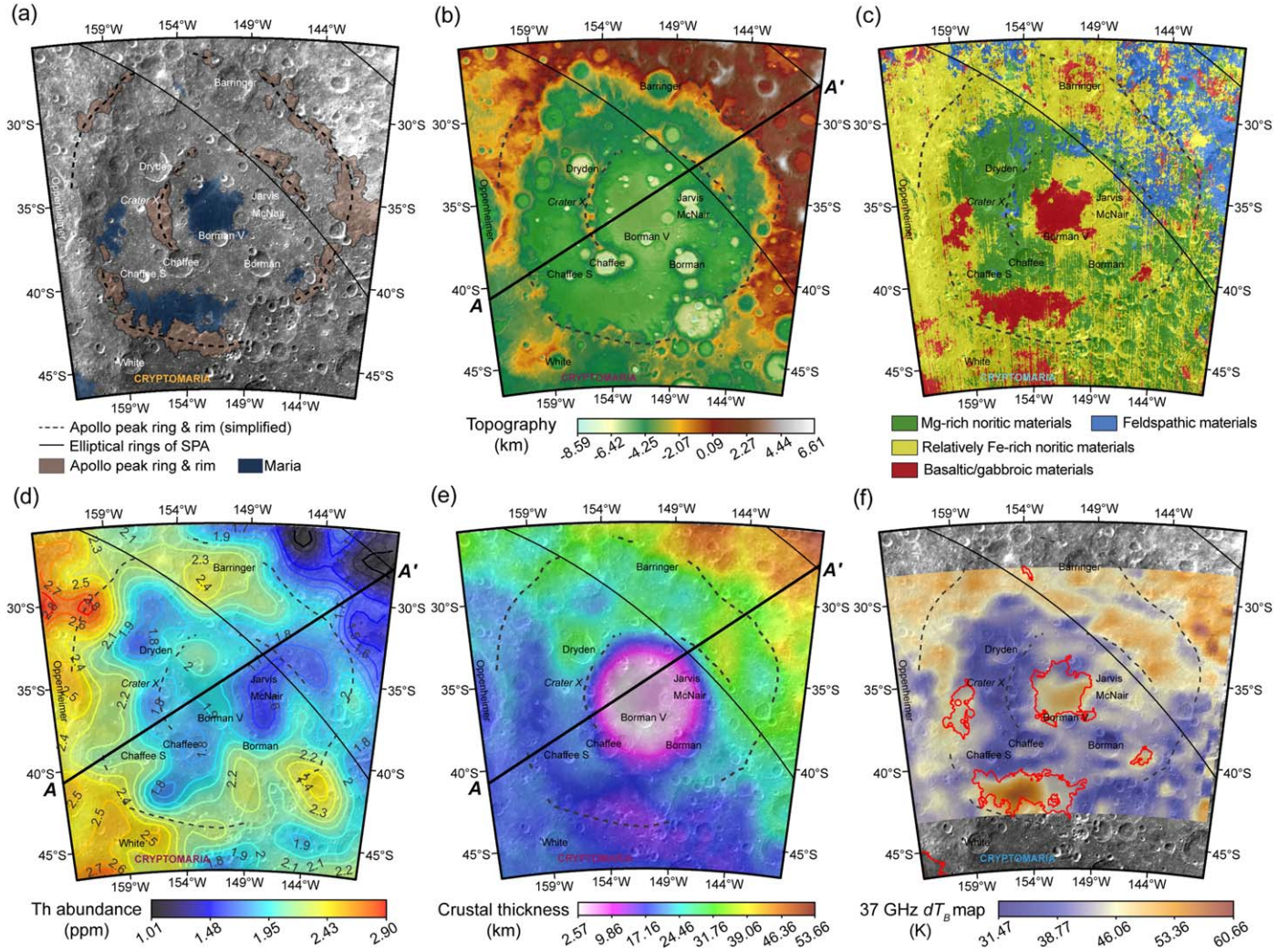

Figure 3. Basic characteristics of the Apollo basin. (a) is the CE-2 DOM image for the Apollo basin (C. Li et al. 2018). The locations of the Apollo peak ring and rim are from M. A. Ivanov et al. (2018). (b) Topographic map from SLDEM2015 (M. K. Barker et al. 2016). (c) Spectral classification based on the M^3 data, see Section 2.2 for details. (d) Thorium distribution around the Apollo basin (D. J. Lawrence et al. 2003). (e) Variations in crustal thickness around Apollo (M. A. Wieczorek et al. 2013). (f) The difference of normalized brightness temperature between noon and dawn (dTB) derived from the CE-2 37 GHz microwave data by Z. Meng et al. (2019). The above panels are in stereographic projection centered at the center of the Apollo basin (36.09°S, 208.52°E; D. M. H. Baker et al. 2011).

Table 2
Spectral Classification Rules Based on the M^3-derived Band Parameters and the Corresponding Interpretations

Spectral Features	Interpretation
$BD_{1\ \mu m} < 0.025$	Feldspathic materials
$BC_{2\ \mu m} < 2\ \mu m$ and $BD_{1\ \mu m} > 0.025$	Mg-rich noritic materials
$2\ \mu m < BC_{2\ \mu m} < 2.15\ \mu m$ and $BD_{1\ \mu m} > 0.025$	Relatively Fe-rich noritic materials
$BC_{2\ \mu m} > 2.15\ \mu m$	Basaltic/gabbroic materials

Note. BC = band center and BD = band Depth.

composition corresponds to othopyroxene or low-Ca clinopyroxene that are close to the ferrosillite endmember in the pyroxene quadrilateral; when the 2 μm is greater than 2.15 μm, the pyroxene corresponds to high-Ca clinopyroxene. As for the band depths, values close to 0 represent a nearly featureless spectrum, indicating a high feldspar content (e.g., D. P. Moriarty & C. M. Pieters 2018). We use 0.025 as the value for the interval: the 1 μm band depth less than this indicates the highly feldspathic material, while the 1 μm band depth greater than this implies a higher abundance of mafic minerals.

Figure 4 shows some examples of the spectra from different geological units in the Apollo basin. The relationship between the 1 and 2 μm band center of a spectrum can reflect the chemical composition of the pyroxene present in the material (e.g., R. L. Klima et al. 2007, 2008, 2011a, 2011b, Figure 4(c)). In the case of the spectra extracted from the Apollo peak ring and southwestern interior of the Apollo basin (shown in green in Figure 4), these spectra display the band centers at relatively short wavelengths (e.g., their 2 μm band centers $<2\ \mu$m). Following the variations of spectral band centers with pyroxene composition (see Figure 13 in R. L. Klima et al. 2011a), this suggests the occurrence of Mg-rich low-Ca pyroxene (including orthopyroxene and parts of low-Ca clinopyroxene), which lithologically corresponds to Mg-rich noritic anorthosite (or anorthositic norite) given the mineral assemblage (Figure 5). Regarding the spectra from the inner- and outer-peak ring Apollo basin floor (shown in yellow in Figure 4), the associated pyroxene composition is slightly richer in Fe and Ca compared

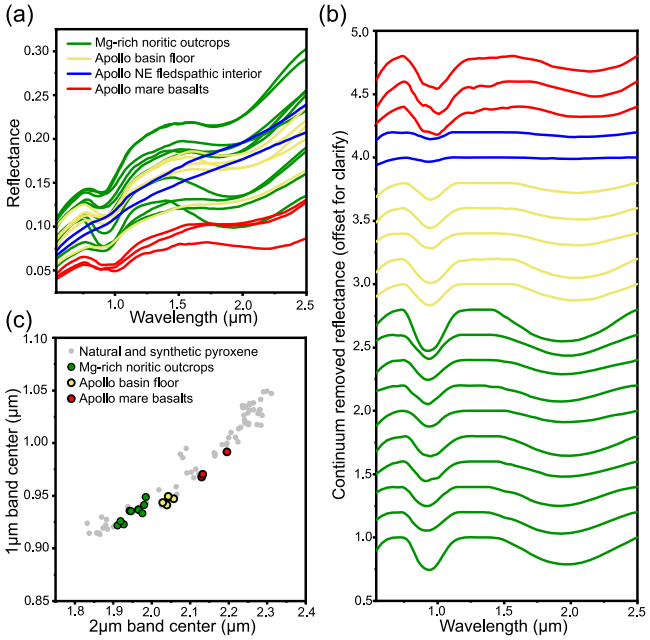

Figure 4. Spectral features of different geological units in the Apollo basin. (a) shows the smoothed M^3 spectra, and their corresponding continuum-removed spectra are present in (b), with an offset of 0.15 between each spectrum. (c) Comparison of band centers between the extracted spectra and the spectra of natural and synthetic pyroxene, the latter points are from D. Liu et al. (2022). The data shown in panel (c) are available as the data behind the figure.

(The data used to create this figure are available in the online article.)

to the previously mentioned spectra, as they display slightly longer-wavelength band centers than those spectra. Yet their rock type is still noritic anorthosite (or anorthositic norite; Figure 5). The spectra from the Apollo mare regions (shown in red in Figure 4) have relatively longer band centers, indicating that they consist of abundant high-Ca clinopyroxene. For those spectra representing more feldspathic materials (shown in blue in Figure 4), they are almost featureless, with the smallest band depths (Figure 4(b)).

3. CE-6 landing Site: The Apollo Peak-ring Basin

3.1. Geological Context of the Apollo Basin

The Apollo peak-ring basin is the largest preserved impact structure within the SPA basin (Figure 1a), centered at 36.09°S, 208.52°E (D. M. H. Baker et al. 2011). M. A. Ivanov et al. (2018) compiled a detailed geological map of the Apollo basin and determined an AMA of $3.98+0.04/-0.06$ Ga for its formation. The Apollo basin extends across two SPA compositional zones defined by D. P. Moriarty & C. M. Pieters (2018), including the "Mg-pyroxene annulus" characterized by abundant Mg-rich pyroxene and the more feldspathic "Heterogenous annulus" (Figure 1(a)). Several specific locations within the Apollo interior (e.g., Dryden crater) indeed exhibit the spectral signatures indicative of bearing Mg-rich low-Ca pyroxene (LCP; N. E. Petro et al. 2010; R. L. Klima et al. 2011b; D. P. Moriarty & C. M. Pieters 2014; S. Yamamoto et al. 2023). Regarding the Apollo peak ring, early investigations based on the multiband spectral data from Clementine (C. M. Pieters et al. 2001) and Kaguya MI (M. Ohtake et al. 2014) suggested that it is composed of anorthosite, while later studies using the hyperspectral Moon Mineralogy Mapper (M^3) data show that the peak ring exhibits a more mafic composition (N. E. Petro et al. 2010; D. M. H. Baker & J. W. Head 2015), distinguishing it from most peak-ring basins on the Moon which are more anorthositic and less mafic (D. M. H. Baker & J. W. Head 2015). The Apollo basin has also created a "depression" in Th abundance (∼2 ppm) relative to the entire SPA basin (Figure 1(a)), possibly as a result of the removal of Th-enriched upper-mantle-derived SPA ejecta during its formation (D. P. Moriarty et al. 2021; J. Zhang et al. 2023).

The Apollo basin floor is partially flooded by mare basalts (shown in red hue in Figure 3(c)), creating a few lava ponds that exhibit a long-lasting volcanic history with AMAs probably ranging from 1.79 to 3.51 Ga (J. Haruyama et al. 2009; J. H. Pasckert et al. 2018; Y. Qian et al. 2024; Y. Wang et al. 2024c). In addition to the varied ages, these mare deposits also show different compositional characteristics. The northwestern and the western mare deposits may be made up by low-Ti basalts (∼2.2− 3.2 wt% TiO_2), and the central and southeastern mare deposits are probably dominated by high-Ti basalts (∼6.2−6.5 wt% TiO_2; C. Orgel et al. 2024; Y. Qian et al. 2024). The southern mare plain, where CE-6 finally landed, is the largest mare deposit within the Apollo basin. This area appears to have a relatively complex geological setting, as the western and eastern parts of this mare plain may belong to two different volcanic units (e.g., J. H. Pasckert et al. 2018; X. Zeng et al. 2023; Y. Qian et al. 2024; Y. Wang et al. 2024c). Compared to the western part, the eastern part may have a slightly older age, and exhibits lower iron and titanium abundances with higher surface albedo. Given that the algorithms for calculating iron (P. G. Lucey et al. 1995, 1998; M. Lemelin et al. 2015) and titanium (H. Sato et al. 2017) abundances has reduced the effect of maturity, it is possible that these variations we observed are related to changes in composition rather than changes in maturity due to space weathering. Y. Qian et al. (2024) interpreted this as representing two episodes of mare eruptions in this area. The earlier low-Ti basalts may have flooded the entire southern mare plain, whereas the high-Ti basalt eruption may have occurred only in the western part, obscuring the preexisting low-Ti basalts. They also attributed the higher albedo observed in the eastern part to a possible higher plagioclase abundance in the basalts. However, it is necessary to mention that the coverage of massive bright ejecta may also lead to the features we see in the eastern part (higher albedo, lower FeO and TiO_2 abundance), as we can observe in the western part where many ejecta rays appear (Figure 2). Those ejecta rays were produced by nearby craters and basins, probably containing higher plagioclse abundance and less mafic abundance relative to the background mare basalts.

The Apollo basin is also characterized by distinct variations in crustal thickness (Figure 3(e); M. A. Wieczorek et al. 2013; D. Guo et al. 2018). Overall, the basin crust in the northeastern (NE) region is 10 km thicker than that in the southwestern (SW) region (Figure 6), and the crustal thickness at the basin center is less than 5 km, which is one of the thinnest crustal locations on the Moon. The volcanic activity within the Apollo basin may be significantly controlled by the crustal thickness variations (Y. Qian et al. 2024), with more mare basalts exposed where the lunar crust is thinner (J. W. Head & L. Wilson 1992, 2017).

Numerical modeling of the Apollo basin event (R. W. K. Potter et al. 2018) suggests that it could be formed

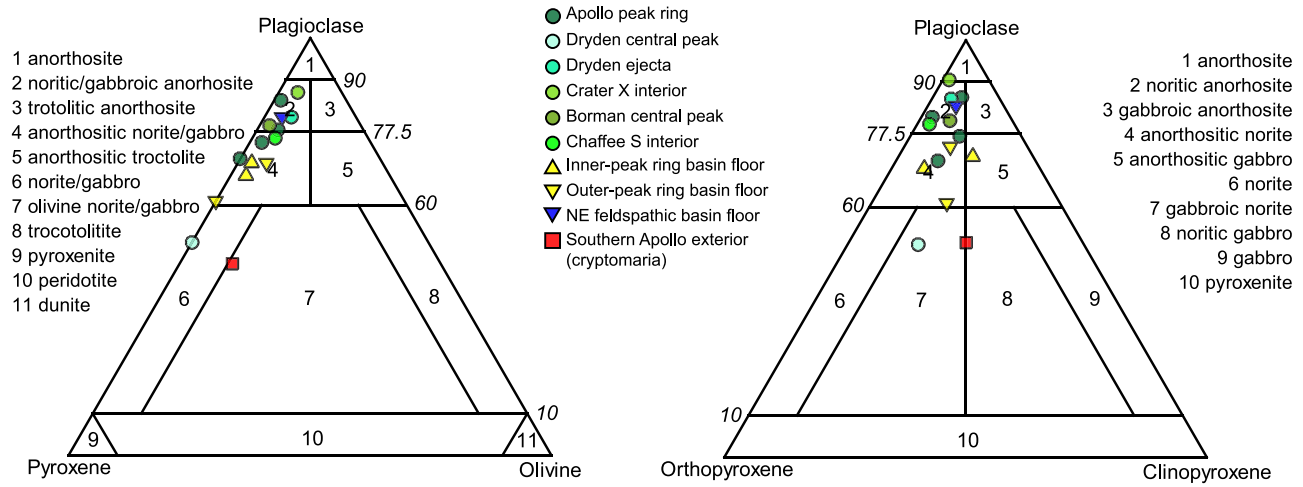

Figure 5. Lithologic identifications of different geological units in the Apollo basin. Corresponding mineral abundances of each point are from MI-derived lunar mineralogy data (M. Lemelin et al. 2015). Ternary diagrams are after D. Stöffler et al. (1980).

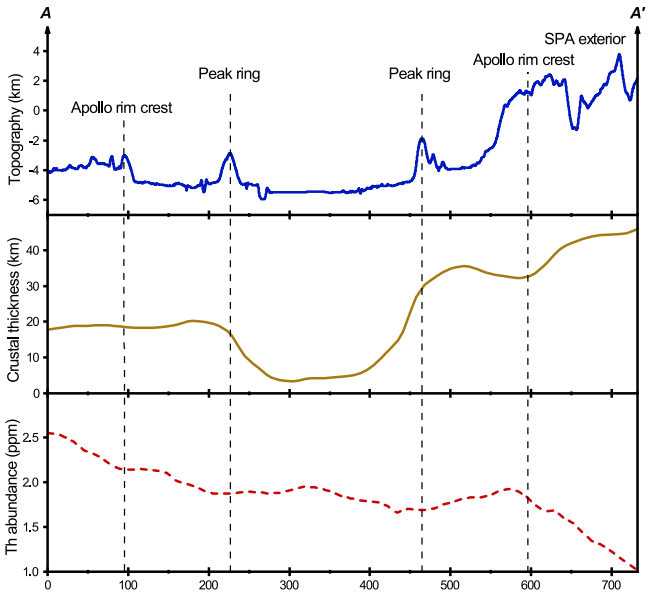

Figure 6. Topography, crustal thickness, and Th abundance variations of the AA' profile. The AA' line is marked in Figures 3(b), (d), and (e).

by impact of a 40 km diameter body traveling at 15 km s^{-1} into 20–40 km thick crustal materials, and that the peak ring material was possibly sourced from depths of 30–70 km, thus possibly comprised of lunar mantle materials, below preimpact highlands primary crust of uncertain thickness. D. M. H. Baker & J. W. Head (2015) also estimated that the maximum depth of excavation for the Apollo basin was about 39 km, providing an upper limit for the depth of origin of the Apollo peak ring.

3.2. Lateral Compositional Variation across the Apollo Basin

Within the Apollo interior, superposed mare basalt deposits are present in only a few patches, and as a result, most premare Apollo basin materials are well exposed and possibly ejected onto the surface CE-6 landing area. These basin materials are thus the focus of our work. As reported in the earlier findings of N. E. Petro et al. (2010), the Apollo basin is generally feldspathic in composition, but includes more mafic materials in mineral assemblage than common farside highlands. Most basin materials exposed in the Apollo interior are lithologically noritic anorthosite or anorthositic norite (Figure 5). Unlike previous spectroscopic studies that are more based on specific point locations (R. L. Klima et al. 2011b; D. P. Moriarty & C. M. Pieters 2014; S. Yamamoto et al. 2023), our spectral classification further reveals a spatial compositional feature of the Apollo basin materials. Here we found a significant lateral difference in mineral composition within the Apollo basin. Due to the spectra displaying notable short band centers (Figure 4(c)), the pyroxene compositions of the noritic anorthosite distributed in the SW portion of the Apollo basin (Figure 3(c)) is more Mg-rich than those observed at the inner- and outer-peak ring basin floor that may be associated with the Apollo impact melt. Their exposures correspond to the localized thin crust (Figure 3(e)). In contrast, the spectra of the NE portion of the Apollo basin and the outward region, where the crust is relative thick, are almost featureless and have the shallowest band depths (Figure 4(b)), implying a higher abundance of feldspathic materials.

Further observations show that the SW portion of the Apollo basin shares similarities with the Apollo basin peak ring in terms of the outcrops of Mg-rich LCP (Figure 3(c)) and a decrease in Th abundance (<2 ppm) compared to the rest of the Apollo basin (Figures 3(d) and 6), although feldspathic abundance is slightly higher in the Apollo peak ring (Figure 5; also see the M^3-derived Integrated Band Depth map in N. E. Petro et al. 2010). On the western side near the peak ring, these Mg-rich materials are likely to be associated with the excavations of some post-Apollo craters, such as Dryden, Chaffee, and Chaffee S. This is also supported by the interpretation from the Chang'E-2 microwave sounder data (Figure 3(f)) that the variations in microwave thermal emission property indicates a shallow surface emplacement of these materials, possibly between 31 and 76.9 cm thick (Z. Meng et al. 2019).

3.3. Foreign Materials Ejected Onto the Surface of the CE-6 Landing Site

Considerable amounts of impact rays with relatively high-albedo can be clearly observed in the grayscale stretched CE-2 orthorectified image (Figure 2(a)), and the areas where they appear correspond to significant decreases in iron and titanium abundances (Figures 2(b), (c)). This implies that, in addition to

the local mare basalts, there is a high possibility that CE-6 can collect some amounts of foreign materials, such as from the peak ring and the southern rim of the Apollo basin, or even beyond. These foreign materials would significantly expand the laboratory studies of the CE-6 samples. Given the possible young age of the CE-6 landing site (see Table 1), only some young Eratosthenian-aged and Copernican-aged impacts could have ejected materials onto the surface of the CE-6 landing site. Z. Yue et al. (2024) used the empirical formula proposed by V. L. Sharpton (2014) to evaluate the thickness of foreign ejecta accumulated at the CE-6 landing site. A total of ∼21.5 cm foreign ejecta thickness was estimated, the majority of which is from Chaffee S (∼16.2 cm), the largest young impact crater near the landing area (Figure 1(b)).

As a major contributor to foreign materials, Chaffee S also displays a slightly different compositional signature. Overall, the materials excavated by Chaffee S are consistent with the Mg-rich LCP-bearing materials distributed elsewhere in the SW portion of the Apollo basin (Figure 3(c)), with the only variation being that it shows a relatively high Th abundance (Figure 3(d)). One possible reason for this could be that the original target region for Chaffee S may have been mixed with Th-rich ejecta from the Oppenheimer crater, which is located on the west of the Apollo basin and younger than the Apollo basin (M. A. Ivanov et al. 2018; C. M. Poehler et al. 2020). The subsequent Chaffee S impact has the potential to eject both the Mg-rich LCP-bearing materials and the Th-rich ejecta from the Oppenheimer basin to the CE-6 landing site.

4. Discussion

4.1. Origin of the Mg-rich Materials and Implications for SPA Stratigraphy

As aforementioned, the striking spatial feature we discovered of the Apollo basin is the SW–NE compositional difference. Mg-rich materials are found predominantly in the SW portion of the basin interior where the crust is thin, as well as in the basin peak ring, essentially coinciding with a decrease in Th content. On the other hand, the NE portion of the basin, as well as the area outside the Apollo basin and the SPA basin, exhibits a composition more akin to the typical lunar feldspathic highlands. If the Apollo impact event removed the Th-elevated pre-Apollo SPA basin deposits as suggested by previous studies (D. P. Moriarty et al. 2021; J. Zhang et al. 2023), then this lateral compositional variation seen within the Apollo basin is likely to provide valuable structural and stratigraphic insights related to SPA basin itself.

The first issue to sort out here is the origin of these Mg-rich materials. Their correlation with the Apollo peak ring implies that, according to the formation mechanism of impact basin peak rings (e.g., P. D. Spudis 1993; M. J. Cintala & R. A. Grieve 1998; G. S. Collins et al. 2002; J. W. Head 2010; D. M. H. Baker et al. 2016; R. W. K. Potter et al. 2018), they could have been sourced from a relatively deep region. These deep-seated materials may have undergone uplift to a shallower depth during the formation of the Apollo peak ring, and then excavated and exposed by subsequent post-Apollo impacts near the peak ring (e.g., Dryden and Chaffee S; Figure 7(b)). In a global investigation of LCP-rich rock bodies, S. Yamamoto et al. (2023) argued that the LCP-bearing materials occurring near the Apollo peak ring could represent the exposure of the ultramafic lunar mantle, which may have layered stucture with olivine-rich layer overlying the LCP-rich layer or a horizonal heterogeneity in composition. The numerical modeling of the Apollo basin (R. W. K. Potter et al. 2018) supports the mantle origin for the peak ring in the case of a thinner crust on the SW side of the Apollo basin. The fact that the crust in the center of the Apollo basin is less than 5 km also demonstrates that the Apollo impact did excavate deep enough. However, an intriguing point we noted is that both the Apollo peak ring and the adjacent Mg-rich materials do not appear to exhibit the anticipated high mafic abundance thought to be characteristic of the lunar mantle (e.g., H. J. Melosh et al. 2017). Instead, the presence of ∼80 wt% plagioclase abundance (Figure 5) in the Apollo peak ring leads us to favor the interpretation of a closer correlation with typical lunar "mafic" lower crust rather than lunar mantle (e.g., M. A. Ivanov et al. 2018). Possibly, as some studies have pointed out (J. W. Head 2010; D. M. H. Baker et al. 2011; D. M. Baker et al. 2012; L. C. Cheek et al. 2013; D. M. H. Baker & J. W. Head 2015; D. M. H. Baker et al. 2016, 2017; G. Xu et al. 2024), the original depth of the basin peak ring materials may be relatively shallow, shallower than its maximum excavation depth.

Under this crust-origin scenario for the Apollo peak ring, we then place the Apollo basin into the context of the whole SPA basin to further investigate the origin of these Mg-rich materials and their implications of the SPA stratigraphic history. I. Garrick-Bethell & M. T. Zuber (2009) documented two elliptical rings of the SPA basin based on topography and compositional distributions (black dashed line in Figure 1(a)). The area between the two ellipses was designated as the Outer Terrace. The Outer Terrace appears to largely correspond to the SPA "heterogenous annulus" (D. P. Moriarty & C. M. Pieters 2018), where feldspathic material dominates, with localized small occurrences of pyroxene-bearing material. When comparing the SPA basin to the Orientale basin, the SPA Outer Terrace is likely equivalent to the Montes Rook Formation in Orientale (X. Wang et al. 2024a), the area between Orientale Cordillera and Outer Rook rings, which could represent a megaterrace possibly formed by the inward collapse of initial basin rim along listric faults at the base of the displaced zone during the latter stage of the multiring basin formation (J. W. Head 2010). If the Outer Rook ring of the Orientale basin can be approximated as its transient cavity rim crest (J. W. Head 1974; C. I. Fassett et al. 2011), we may similarly assume the smaller identified ellipse of SPA can approximate the size of the SPA transient cavity, then this Outer Terrace is positioned outside the SPA transient cavity, probably covered primarily by the basin ejecta excavated from the transient cavity (J. W. Head 2010; Figure 7(a)). A first-order thickness estimate of the SPA ejecta deposited onto the SPA Outer Terrace is presented here using the ejecta decay model proposed by C. I. Fassett et al. (2011), which was developed based on the morphometric measurements of the Orientale basin and is suitable for the ejecta thickness estimate of large impact basins (e.g., A. S. Krasilnikov et al. 2024):

$$t = 2900\left(\frac{r}{R}\right)^{-2.8} \text{ (in meter)},$$

where t is the ejecta thickness at a distance r from the basin center, R is the rim-crest radius of the basin. We treated the two SPA elliptical rings proposed by I. Garrick-Bethell & M. T. Zuber (2009) as representative of the size of the SPA

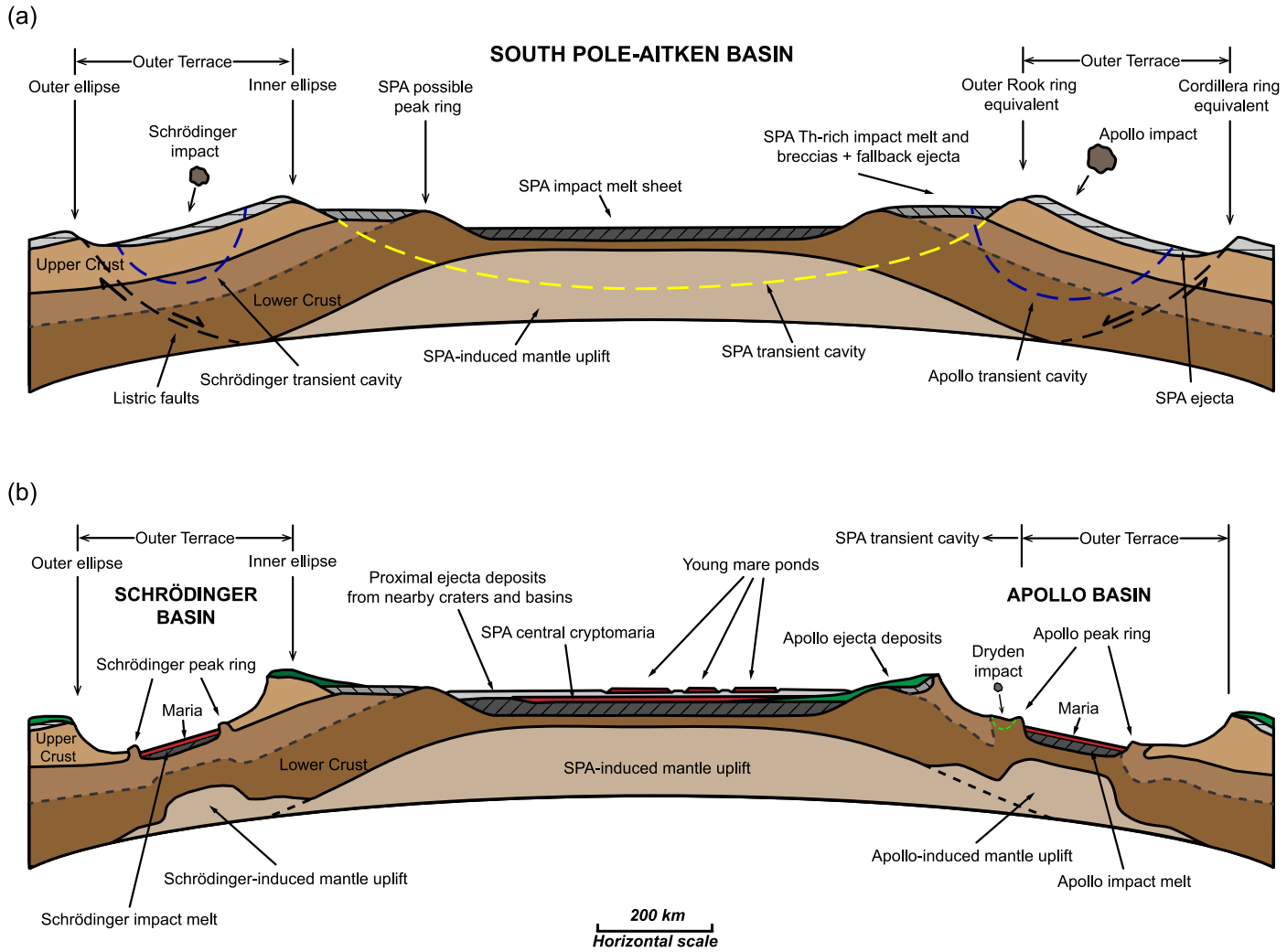

Figure 7. Schematic cross-sectional diagrams of SPA basin structure, (a) pre- and (b) post-Apollo/Schrödinger events. The horizontal scale of the diagrams corresponds to the actual topographic scale. The stratigraphy in the SPA basin center is referenced to Figure 12 in X. Wang et al. (2024a).

transient cavity and the SPA basin, respectively, for estimating the thickness of ejecta at the SPA transient cavity's rim, which is ∼5.3−7.9 km. This could provide the maximum SPA ejecta thickness deposited onto the SPA Outer Terrace and can indeed be penetrated through by the Apollo basin (∼39 km excavation depth suggested by D. M. H. Baker & J. W. Head 2015). As shown in Figures 1(a) and 3(a), the ∼492 km diameter Apollo basin has only its NE portion located within the SPA Outer Terrance, while its SW portion extends into the range of the SPA transient cavity. This may lead to a deeper overall excavation depth in the SW interior of the Apollo basin compared to the NE interior, and account for the SW–NE variations in compositional distribution and crustal thickness that we observed in the Apollo basin (Figures 3(c), (e)).

We also compare the Apollo basin with the Schrödinger basin, another large basin located in the other corner of the SPA basin (Figure 1(a)), to assess the potential pre-SPA stratified lithologies of the SPA target crust. The Schrödinger peak-ring basin with a diameter of ∼329 km (D. M. H. Baker et al. 2011) is smaller in size than the Apollo basin and lies exclusively within the SPA Outer Terrace (Figure 1(a)). D. A. Kring et al. (2016) suggested the sampling depth of the Schrödinger peak ring is no deeper than 30 km. Such a depth indicates that the Schrödinger impact could also be able to penetrate through the SPA ejecta deposited on the Outer Terrace (∼5.3−7.9 km), exposing and sampling the pre-SPA basin crust, but likely not reaching the mantle. The overall sampling of the Schrödinger basin may be comparable to the more feldspathic NE interior of the Apollo basin, as they are both situated within the SPA Outer Terrace (Figure 7). However, the excavation depth of the Schrödinger peak ring should be shallower than that of the Apollo peak ring. The peak ring of the Schrödinger basin is one of two sites where olivine-bearing materials were found across the entire SPA basin, the other being the central peak of the Zeeman crater (S. Yamamoto et al. 2010, 2012; G. Y. Kramer et al. 2013, Figure 1(a)). In contrast, no evidence of olivine-bearing materials has been found in the peak ring of the Apollo basin with deeper excavation, which instead contains Mg-rich LCP materials (R. L. Klima et al. 2011b; S. Yamamoto et al. 2023). If this is the case, assuming the stratigraphy of the SPA impact target is homogeneous on the large scale, we may hypothesize that the emplacement of olivine-bearing materials in local stratigraphy is shallower than the LCP-bearing materials. This stratigraphic relationship appears to be common on a global scale according to the global spectral investigation by S. Yamamoto et al. (2023), while they interpreted that these olivine- and LCP-bearing materials are the constituents of the

lunar mantle. They pointed out that mantle overturn (e.g., P. C. Hess & E. M. Parmentier 1995) may explain its inconsistency with the early crystallization sequence of the Lunar Magma Ocean. However, in this work, we favor interpreting these materials as more related to a crustal origin due to their close proximity to feldspathic materials, at least within the SPA basin, suggesting that they may represent crustal troctolitic and noritic materials (e.g., P. Lucey 2010, Figure 5). These materials could be the product of Mg-suite intrusion during the lunar secondary crust building (e.g., C. K. Shearer et al. 2015; see Section 4.2 in detail), and the cause of this observed stratigraphic relationship is possibly related to the varying composition of the Mg-suite parent magma or the different depths of each intrusion. At present, this remains an important open question, and we expect that the CE-6 samples collected from the Apollo basin will provide some significant clues. There is also a great need for future samples collected from the Schrödinger basin (e.g., Endurance mission concept; J. T. Keane et al. 2022), and as discussed in this work, their comparison with the Apollo Basin samples will provide data for reconstructing the SPA vertical stratigraphic profile and history and to test these hypotheses above.

4.2. The Role of KREEP During the Lunar Secondary Crust Building

Our analysis suggests the presence of deep crustal materials within the Apollo basin. The overall low Th abundance throughout the basin indicates that these exposures are low in Th. Furthermore, our investigation reveals a further decrease in Th abundance associated with the occurrence of the Mg-rich materials, including the Apollo peak ring (Figures 3(d) and 6). If such materials are representative of the local lunar lower crust and Th can be representative of the KREEP (potassium, rare-earth elements, and phosphorus) component as usually understood, in view of their characteristics of containing Mg-rich LCP, they could be good candidates for Mg-suite plutons (e.g., R. L. Klima et al. 2011b; C. K. Shearer et al. 2015) produced during lunar secondary crust building, and with a low KREEP concentration. This implies that no significant KREEP component was assimilated during their formation, although the direct correlation between the regional Th concentrations and nonmare mafic lithologies within the SPA basin suggests that those incompatible trace elements (ITEs) in the SPA is indigenous to the basin itself (e.g., I. Garrick-Bethell & M. T. Zuber 2005; J. J. Hagerty et al. 2011), whose source may have been in place prior to the formation of the SPA basin (e.g., J. J. Hagerty et al. 2011; D. P. Moriarty et al. 2021; J. Zhang et al. 2023).

Most of Apollo Mg-suite samples were collected within the Procellarum KREEP Terrane and contain elevated concentrations of a KREEP component, which may lead to overestimation of the importance of KREEP in producing Mg-suite parental melts. As T. C. Prissel et al. (2023) recently pointed out, it is possible that early lunar secondary crust building may not have required the contribution of other energy sources such as KREEP. Such low KREEP Mg-rich clasts were found in the Chang'E-5 returned samples (Q. He et al. 2023). Some studies have proposed a hypothesis that the giant SPA impact event could have served to transfer a farside basal crust KREEP layer to the nearside through hemisphere-scale mantle convection over the course of >200 Ma after the SPA impact (e.g., J. J. Hagerty et al. 2011; M. J. Jones et al. 2022; N. Zhang et al. 2022). This might be one of the potential reasons for KREEP-poor Mg-suite being excavated by the post-SPA Apollo basin. In addition, understanding the timing of lunar secondary crust building is also important. Indeed, there is an overlap in age between returned Mg-suite samples (4.5 to 4.1 Ga; M. A. Wieczorek et al. 2006) and SPA formation (∼4.2−4.3 Ga H. Hiesinger et al. 2012). If the KREEP-poor Mg-suite observed in the Apollo basin was formed after the formation of SPA, this would extend the timeline of lunar secondary crust building. Therefore, CE-6 sampling in the Apollo basin could test these hypotheses, ascertain KREEP-poor Mg-suite chronology, and clarify whether KREEP plays a pivotal role in Mg-suite petrogenesis during lunar secondary crust formation.

4.3. Potential Lithologically Diverse Farside Sample Returned by CE-6

On the basis of the above synthesis of the Apollo basin where CE-6 landed, we can make the following preliminary prediction of the lithological types that CE-6 may have been able to sample.

1. Local mare basalts: the CE-6 landing site is located within the southern mare plain of the Apollo basin, thus local mare basalts should be the dominant lithological type in the collected samples. These first-sampled farside basalts will provide insight into the nature of the farside lunar mantle. Moreover, if the basalts here are as young as the measurements from the CSFD analysis (Table 1), why do they have different composition compared to the nearside young Eratosthenian mare basalts represented by CE-5 (at least from the perspective of orbital remote sensing; e.g., D. Liu et al. 2022; Y. Qian et al. 2024)? What is the heating source of the young farside mare basalts?
2. Mg-rich noritic materials: as we discussed in Section 4.1, the type of lithologies, if found in the CE-6 samples, could be representative of the constituents from local farside lower crust and correlated with Mg-suite plutons formed during lunar secondary crust building. Given that these deep-seated materials may have undergone uplift to a shallower depth during the Apollo basin formation event and then excavated and exposed by subsequent post-Apollo impacts, perhaps they may aid in constraining the age of the Apollo basin. In addition, their low KREEP feature may also help clarify whether KREEP plays a pivotal role in Mg-suite petrogenesis during lunar secondary crust formation (e.g., C. K. Shearer et al. 2015; T. C. Prissel et al. 2023).
3. ITEs-rich materials: Our findings in this work suggest that the Apollo basin materials may lack Th components. The impact that created the Apollo basin also appears to have removed local preexisting Th-rich materials (e.g., D. P. Moriarty et al. 2021; J. Zhang et al. 2023). If this is the case, any presence of Th-rich or ITEs-rich materials in the CE-6 returned samples likely indicates a mixture of materials from outside the Apollo basin, perhaps directly related to the SPA basin itself. Indeed, as we mentioned in Section 3.3, Chaffee S does have the potential to eject the Th-elevated material onto the surface of CE-6 landing site, which may have originally sourced from the Th-rich ejecta of the Oppenheimer crater. However, the origin of Th within the SPA basin remains uncertain.

D. P. Moriarty et al. (2021) suggested that these Th-rich materials could represent the upper-mantle-derived SPA ejecta exposed during the formation of the SPA basin, because they found that the crescent-shaped elevation in Th abundance across SPA is similar to the distribution of the upper-mantle-derived (i.e., urKREEP) ejecta predicted by three-dimensional models of the SPA-forming impact (H. J. Melosh et al. 2017). SPA impact melt sheet could also be one possible source, which is inferred to be ITEs-rich after differentiation (W. M. Vaughan & J. W. Head 2014). Although the existence of KREEP basalts has not been demonstrated on the farside of the moon, their emplacement within the SPA basin is still possible (P. D. Spudis 1979), especially given the ancient age of the basin. Related to this is the possibility of Mg-suite magmatic intrusion occurring early in the SPA evolution (J. J. Hagerty et al. 2011). If the Mg-suite parental magma assimilated the KREEP component during ascent, forming the KREEP-rich crustal materials, subsequent impacts inside the SPA could also have produced ITEs-rich ejecta. All these hypotheses could be tested if such lithologies can be found in the CE-6 samples, which are likely to contain key information about SPA evolution, including its age.

4.4. Implications of CE-5 Sample Analysis for CE-6

CE-5 has returned the new lunar samples for laboratory research, 48 years after the end of the Apollo program. Compared to the Apollo era, there have been significant advances in analysis technology, particularly the wider application of in situ microarea analysis techniques such as Electron probe microanalyzer and Secondary ion mass spectrometry (J. H. Li et al. 2022b). Bulk soil studies of the Apollo soil samples have mostly used the techniques such as instrumental neutron activation analysis (INAA) and X-ray fluorescence spectrometer (XRF; e.g., D. W. Beaty et al. 1979), which can cause damage to the samples or require complete melting, resulting in a large sample mass loss. Comparatively, the samples collected by the CE-5 mission need to constrain a large-scale mass loss due to the limited weight. The soil particles in the CE-5 samples are also finer than those in Apollo samples (S. Zhao et al. 2023). Therefore, apart from some initial studies of the overall characteristics of the CE-5 samples using INAA and XRF (e.g., C. Li et al. 2022a), most studies have been conducted based on in situ microarea techniques for analyzing individual mineral particles and glass beads (e.g., S. Hu et al. 2021; Q. L. Li et al. 2021; H.-C. Tian et al. 2021). The total weight of samples collected by the CE-6 mission (~1935.3 g) is similar to that of CE-5 (~1731 g), and it is anticipated that in situ microarea techniques will also be widely used for the laboratory analysis of CE-6 samples. However, it is important to note that because of the relatively purity of the soil in the CE-5 landing site (Y. Qian et al. 2021), the results of laboratory in situ analysis can be well matched with the bulk soil analysis. In contrast, based on the analysis in this work, the lunar soil collected from CE-6 may contain relatively more foreign materials than those in the CE-5 samples. The potential diversity of CE-6 samples may lead to differences between laboratory in situ microarea analysis results and bulk soil analysis.

5. Conclusions

China's CE-6 mission represents a significant milestone in lunar exploration, marking the first successful retrieval of samples from the farside of the Moon. Landing in the southern mare plain of the Apollo basin within the SPA Basin, CE-6 has provided an unprecedented opportunity to study the geological and compositional diversity of this enigmatic region. Our study has focused on the geological context and compositional variations within the Apollo basin, with an emphasis on the basin materials that CE-6 may have collected. We have observed that the Apollo basin exhibits a significant lateral compositional variation, with Mg-rich materials predominantly in the SW with thinner crust and more feldspathic materials in the NE with thicker crust. We place the Apollo basin into the context of the entire SPA basin and then attribute this lateral heterogeneity to the fact that the Apollo basin is situated on different structures of the underlying SPA basin. The Mg-rich noritic materials that occur in the SW interior of the Apollo basin are interpreted to represent deep-seated lithologies of local lower crust, probably originating from the Mg-suite plutons formed during lunar secondary crust building. The low Th abundance associated with these materials further suggests a KREEP-poor origin, challenging the traditional view of the role of KREEP in Mg-suite petrogenesis. We also draw specific comparisons between the Apollo Basin and the Schrödinger Basin, noting that samples from both basins will aid in understanding the stratigraphy of the SPA basin.

Based on our synthesis of the geological context of the CE-6 landing site, we believe that, in addition to the local mare basalt, significant amounts of foreign materials including Mg-rich noritic materials associated with the Apollo basin and Th-rich materials originating from the SPA basin could be sampled by CE-6. It is expected that samples of all of these lithological types will open a new chapter in lunar science, providing immediate opportunities for detailed exploration of the lunar farside and potentially shedding light on some outstanding questions such as the history of the SPA basin (e.g., D. P. Moriarty et al. 2021), the compositional characteristics of the lunar deep interior (e.g., H. J. Melosh et al. 2017), as well as the substantial asymmetry between the lunar nearside and farside in mare deposits, topography, crustal thickness, and compositional terrane types (e.g., J. Head et al. 2024).

Acknowledgments

We would like to gratefully acknowledge very useful and informative discussions with Dr. Carle Pieters (Brown University) and Dr. Sergey Krasilnikov (the Hong Kong Polytechnic University). We also thank Dr. Zhiguo Meng (Jilin University) for providing us with the brightness temperature map of the Apollo basin derived from CE-2 micriowave data. This study was undertaken while X. W. was a Visiting Graduate Student at Brown University, supported by an International Cooperation Training Program from the University of Chinese Academy of Sciences. This work was supported by the grants from the National Natural Science Foundation of China (NSFC; grant Nos. 12373068 and 42371384) and the Research Grants Council of Hong Kong (Project No: R5043-19). All raw data used in this study are available in the NASA Planetary Data System (PDS; https://pds-geosciences.wustl.edu/), expect the CE-2 DOM image that can be accessed at China's Lunar and Planetary Data Release System (https://moon.bao.ac.cn/web/enmanager/home).

ORCID iDs

Xing Wang https://orcid.org/0000-0001-7428-2360
James W. Head https://orcid.org/0000-0003-2013-560X
Wenhao Zhao https://orcid.org/0000-0002-9271-0821
Yuan Chen https://orcid.org/0000-0002-7814-5264
Qin Zhou https://orcid.org/0000-0001-8562-9737
Jiaming Zhu https://orcid.org/0009-0001-0507-8531
Bo Wu https://orcid.org/0000-0001-9530-3044
Chunlai Li https://orcid.org/0000-0002-0817-2742

References

Baker, D. M., Head, J. W., Neumann, G. A., Smith, D. E., & Zuber, M. T. 2012, JGRE, 117, E00H16
Baker, D. M. H., & Head, J. W. 2015, Icar, 258, 164
Baker, D. M. H., Head, J. W., Collins, G. S., & Potter, R. W. K. 2016, Icar, 273, 146
Baker, D. M. H., Head, J. W., Fassett, C. I., et al. 2011, Icar, 214, 377
Baker, D. M. H., Head, J. W., Phillips, R. J., et al. 2017, Icar, 292, 54
Barker, M. K., Mazarico, E., Neumann, G. A., et al. 2016, Icar, 273, 346
Beaty, D. W., Hill, S. M. R., Albee, A. L., Ma, M. S., & Schmitt, R. A. 1979, in Proc. of 10th Lunar and Planetary Science Conf. (New York: Pergamon Press), 41
Boardman, J. W., Pieters, C. M., Green, R. O., et al. 2011, JGRE, 116, E00G14
Cheek, L. C., Donaldson Hanna, K. L., Pieters, C. M., Head, J. W., & Whitten, J. L. 2013, JGRE, 118, 1805
Cintala, M. J., & Grieve, R. A. 1998, M&PS, 33, 889
Clark, R. N., & Roush, T. L. 1984, JGRB, 89, 6329
Collins, G. S., Melosh, H. J., Morgan, J. V., & Warner, M. R. 2002, Icar, 157, 24
Fassett, C. I., Head, J. W., Smith, D. E., Zuber, M. T., & Neumann, G. A. 2011, GeoRL, 38, L17201
Garrick-Bethell, I., & Zuber, M. T. 2005, GeoRL, 32, L13203
Garrick-Bethell, I., & Zuber, M. T. 2009, Icar, 204, 399
Greeley, R., Kadel, S. D., Williams, D. A., et al. 1993, JGRE, 98, 17183
Green, R. O., Pieters, C., Mouroulis, P., et al. 2011, JGRE, 116, E00G19
Guo, D., Liu, J., Head, J. W., et al. 2018, JDSE, 5, 488
Hagerty, J. J., Lawrence, D. J., & Hawke, B. R. 2011, JGRE, 116, E06001
Haruyama, J., Ohtake, M., Matsunaga, T., et al. 2009, Sci, 323, 905
He, Q., Cao, Z., Qian, Y., et al. 2023, Icar, 408, 115853
Head, J., Wang, X., Lark, L., Wilson, L., & Qian, Y. 2024, in 55th Lunar and Planetary Science Conf. (The Woodlands, TX: LPI Contribution), 1459
Head, J. W. 1974, Moon, 11, 327
Head, J. W. 2010, GeoRL, 37, L02203
Head, J. W., & Wilson, L. 1992, GeCoA, 56, 2155
Head, J. W., & Wilson, L. 2017, Icar, 283, 176
Hess, P. C., & Parmentier, E. M. 1995, E&PSL, 134, 501
Hiesinger, H., Jaumann, R., Neukum, G., & Head, J. W. 2000, JGRE, 105, 29239
Hiesinger, H., van der Bogert, C. H., Pasckert, J. H., et al. 2012, in 43rd Lunar and Planetary Science Conf. (The Woodlands, TX: LPI Contribution), 2863
Hu, S., He, H., Ji, J., et al. 2021, Natur, 600, 49
Ivanov, M. A., Hiesinger, H., van der Bogert, C. H., et al. 2018, JGRE, 123, 2585
Jia, Z., Chen, J., Kong, J., et al. 2024, Icar, 416, 116107
Jones, M. J., Evans, A. J., Johnson, B. C., et al. 2022, SciA, 8, eabm8475
Keane, J. T., Tikoo, S. M., Elliott, J. O., et al. 2022, in 2022 Annual Meeting of the Lunar Exploration Analysis Group (The Woodlands, TX: LPI Contribution), 5031
Klima, R. L., Dyar, M. D., & Pieters, C. M. 2011a, M&PS, 46, 379
Klima, R. L., Pieters, C. M., Boardman, J. W., et al. 2011b, JGRE, 116, E00G06
Klima, R. L., Pieters, C. M., & Dyar, M. D. 2007, M&PS, 42, 235
Klima, R. L., Pieters, C. M., & Dyar, M. D. 2008, M&PS, 43, 1591
Kramer, G. Y., Kring, D. A., Nahm, A. L., & Pieters, C. M. 2013, Icar, 223, 131
Krasilnikov, A. S., Ivanov, M. A., Krasilnikov, S. S., & Head, J. W. 2024, Icar, 420, 116190
Kring, D. A., Kramer, G. Y., Collins, G. S., Potter, R. W. K., & Chandnani, M. 2016, NatCo, 7, 13161
Lawrence, D. J., Elphic, R. C., Feldman, W. C., et al. 2003, JGR, 108, 5102
Lemelin, M., Lucey, P. G., Song, E., & Taylor, G. J. 2015, JGRE, 120, 869
Lemelin, M., Lucey, P. G., Miljkovic, K., et al. 2019, P&SS, 165, 230
Li, C., Hu, H., Yang, M., et al. 2024, Natl. Sci. Rev., 11, nwae328
Li, C., Hu, H., Yang, M. F., et al. 2022a, Natl. Sci. Rev., 9, nwab188
Li, C., Liu, J., Ren, X., et al. 2018, Geogr. Inf. Sci., 43, 485
Li, J. H., Yang, W., Li, X. Y., & He, Y. S. 2022b, AtSpe, 43, 1
Li, Q. L., Zhou, Q., Liu, Y., et al. 2021, Natur, 600, 54
Liu, D., Wang, X., Liu, J., et al. 2022, NatCo, 13, 5965
Lucey, P. 2010, NatGe, 3, 517
Lucey, P. G., Blewett, D. T., & Hawke, B. R. 1998, JGRE, 103, 3679
Lucey, P. G., Taylor, G. J., & Malaret, E. 1995, Sci, 268, 1150
Melosh, H. J., Kendall, J., Horgan, B., et al. 2017, Geo, 45, 1063
Meng, Z., Wang, Y., Chen, S., et al. 2019, IJSTA, 12, 2575
Moriarty, D. P., & Pieters, C. M. 2014, in 45th Lunar and Planetary Science Conf. (The Woodlands, TX: LPI Contribution), 2516
Moriarty, D. P., & Pieters, C. M. 2018, JGRE, 123, 729
Moriarty, D. P., Watkins, R. N., Valencia, S. N., et al. 2021, JGRE, 126, e2020JE006589
Nelson, D. M., Koeber, S. D., Daud, K., et al. 2014, in 45th Lunar and Planetary Science Conf. (The Woodlands, TX: LPI Contribution), 2861
Neukum, G. 1983, PhD thesis, University of Munich
Neukum, G., Ivanov, B. A., & Hartmann, W. K. 2001, in Chronology and Evolution of Mars: Proc. of an ISSI Workshop (Cham: Springer), 55
Ohtake, M., Haruyama, J., Matsunaga, T., et al. 2008, EP&S, 60, 257
Ohtake, M., Uemoto, K., Yokota, Y., et al. 2014, GeoRL, 41, 2738
Orgel, C., Torres, I., Besse, S., et al. 2024, PSJ, 5, 29
Pasckert, J. H., Hiesinger, H., & van der Bogert, C. H. 2018, Icar, 299, 538
Petro, N. E., & Pieters, C. M. 2004, JGRE, 109, E06004
Petro, N. E., Sunshine, J., Pieters, C., et al. 2010, in 41st Annual Lunar and Planetary Science Conf. (The Woodlands, TX: LPI Contribution), 1802
Pieters, C. M., Boardman, J., Buratti, B., et al. 2009, CSci, 96, 500
Pieters, C. M., Head, J. W., Gaddis, L., Jolliff, B., & Duke, M. 2001, JGRE, 106, 28001
Poehler, C. M., Ivanov, M. A., van der Bogert, C. H., et al. 2020, in Europlanet Science Congress 2020, Vol. 14 (Brussels: Europlanet Society), EPSC2020–600
Potter, R. W. K., Head, J. W., Guo, D., Liu, J., & Xiao, L. 2018, Icar, 306, 139
Prissel, T. C., Zhang, N., Jackson, C. R. M., & Li, H. 2023, NatCo, 14, 5002
Qian, Y., Head, J., Michalski, J., et al. 2024, E&PSL, 637, 118737
Qian, Y., Xiao, L., Wang, Q., et al. 2021, E&PSL, 561, 116855
Sato, H., Robinson, M. S., Lawrence, S. J., et al. 2017, Icar, 296, 216
Savitzky, A., & Golay, M. J. E. 1964, AnaCh, 36, 1627
Sharpton, V. L. 2014, JGRE, 119, 154
Shearer, C. K., Elardo, S. M., Petro, N. E., Borg, L. E., & McCubbin, F. M. 2015, AmMin, 100, 294
Spudis, P. D. 1979, in Conference on The Lunar Highlands Crust, Vol. 394 (The Woodlands, TX: LPI Contribution), 157
Spudis, P. D. 1993, The Geology of Multi-ring Impact Basins (Cambridge: Cambridge Univ. Press)
Spudis, P. D., Gillis, J. J., & Reisse, R. A. 1994, Sci, 266, 1848
Stöffler, D., Knöll, H. D., Marvin, U. B., Simonds, C. H., & Warren, P. H. 1980, in Conf. Lunar Highlands Crust (New York: Pergamon Press), 51
Tian, H.-C., Wang, H., Chen, Y., et al. 2021, Natur, 600, 59
Vaughan, W. M., & Head, J. W. 2014, P&SS, 91, 101
Wang, X., Head, J. W., Chen, Y., et al. 2024a, JGRE, 129, e2023JE008176
Wang, X., Head, J. W., Qian, Y., et al. 2024b, in 55th Lunar and Planetary Science Conf. (The Woodlands, TX: LPI Contribution), 1873
Wang, Y., Nan, J., Zhao, C., et al. 2024c, RemS, 16, 2024
Whitten, J. L., & Head, J. W. 2015, Icar, 247, 150
Wieczorek, M. A., Jolliff, B. L., Khan, A., et al. 2006, RvMG, 60, 221
Wieczorek, M. A., Neumann, G. A., Nimmo, F., et al. 2013, Sci, 339, 671
Xu, G., Zhu, M., Luo, X., Ding, M., & Wünnemann, K. 2024, in 55th Lunar and Planetary Science Conf. (The Woodlands, TX: LPI Contribution), 1444
Yamamoto, S., Nagaoka, H., Ohtake, M., et al. 2023, JGRE, 128, e2023JE007817
Yamamoto, S., Nakamura, R., Matsunaga, T., et al. 2010, NatGe, 3, 533
Yamamoto, S., Nakamura, R., Matsunaga, T., et al. 2012, Icar, 218, 331
Yue, Z., Di, K., Wan, W., et al. 2022, NatAs, 6, 541
Yue, Z., Gou, S., Sun, S., et al. 2024, Innov, 5, 100663
Zeng, X., Liu, D., Chen, Y., et al. 2023, NatAs, 7, 1188
Zhang, J., Head, J. W., Liu, J., & Potter, R. W. 2023, RemS, 15, 1861
Zhang, N., Ding, M., Zhu, M.-H., et al. 2022, NatGe, 15, 37
Zhao, S., Xiao, L., Qian, Y., et al. 2023, Icar, 406, 115766
Zhou, C., Jia, Y., Liu, J., et al. 2022, AdSpR, 69, 823
Zuber, M. T., Smith, D. E., Watkins, M. M., et al. 2013, Sci, 339, 668